Nanoscale

PAPER

View Article Online
View Journal | View Issue

Check for updates

Cite this: *Nanoscale*, 2025, **17**, 13708

Tri-spectral decoupled programmable thermal emitter for multimode camouflage with heterogeneous phase-change integration†

Sihong Zhou, [a,b,c] Shikui Dong,[a,b] Jiameng Song,[a,b] Yanming Guo, [a,b] Yong Shuai *[a,b] and Guangwei Hu *[c,d]

Camouflage technology requires tailoring of the optical characteristics of objects against possible detection. Currently, there are three essential spectra, namely, 0.36–0.83 μm, 3–5 μm, and 8–14 μm, corresponding to the commonly used visible camera and thermal detectors. Thus, to fulfil the mentioned requirement, herein, we present the efficient design and optimization of a tri-spectral decoupled thermal emitter using a heterogeneous integrated phase-change material (PCM) multilayer composed of vanadium dioxide (VO_2) and In_3SbTe_2 (IST). This thermal emitter could theoretically feature both structural colors across the visible range and independently programmable emissivity modulation with up to 80% absolute tuning in two infrared detection regions. Additionally, two methods for achieving confusing and deceptive colored thermal camouflage are proposed based on this thermal emitter, enhancing camouflage disorientation capabilities and enabling the generation of deceptive infrared images that mimic other objects. Thus, this work offers a near-perfect solution with flexible designs for camouflage in complex environments.

Received 27th January 2025,
Accepted 23rd April 2025

DOI: 10.1039/d5nr00385g

rsc.li/nanoscale

1. Introduction

Visible (VIS) and infrared (IR) scattering fingerprints are crucial for detection systems to identify targets, while camouflage aims to disable or confuse these detectors. Many animals can adjust their VIS properties to blend with their surroundings,[1,2] inspiring researchers to engineer IR spectral characteristics for thermal camouflage that mimic dynamic environmental conditions. Recently, advancements have been made in tailoring optical characteristics using multilayer photonic crystals,[3,4] porous nanostructures,[5,6] and bionic designs.[7,8] However, conventional passive materials cannot dynamically regulate their thermal radiation properties owing to their static electronic density of states, limiting their capability to adapt to complex and changing environments.[9–11] Active materials, such as the phase change material VO_2, enable thermal camouflage devices to control their thermal radiation characteristics. However, current VO_2-integrated thermal camouflage devices often require specialized metal microstructures for selective spectral control,[12–14] limiting their large-scale production. Additionally, emissivity gradient control by VO_2 through temperature changes can only be achieved within the temperature range near the phase transition temperature, and the non-volatile phase change process demands continuous energy supply, making these devices unsuitable for targets with wide temperature ranges. Furthermore, current active thermal emitters based on phase-change materials, such as VO_2,[15,16] $Ge_2Sb_2Te_5$,[17,18] and IST,[19,20] have demonstrated potential for single- or dual-band emissivity modulation, but fully decoupled multispectral tunable thermal camouflage should be prioritized for its superior adaptability to natural environments. For example, in forests, leaves change color from spring to autumn, and their emissivity in the range of 3–5 μm decreases as their water content diminishes, while their emissivity in the range of 8–14 μm remains relatively stable.[21,22] Fig. 1a and b illustrate a vivid schematic, where an ideal gray body model is adopted, and the apparent temperature is calculated using eqn (1). Considering solar and environmental radiation, the thermal radiation characteristics of low-temperature objects are primarily influenced by emissivity in the range of 3–5 μm, with

---

[a] Key Laboratory of Aerospace Thermophysics of Ministry of Industry and Information Technology, Harbin 150001, China. E-mail: shuaiyong@hit.edu.cn
[b] School of Energy Science and Engineering, Harbin Institute of Technology, Harbin 150001, China
[c] School of Electrical and Electronic Engineering, 50 Nanyang Avenue; Nanyang Technological University, Singapore, 639798, Singapore.
E-mail: guangwei.hu@ntu.edu.sg
[d] CNRS-International-NTU-Thales Research Alliance (CINTRA), IRL 328850 Nanyang Drive, Singapore 637553, Singapore

† Electronic supplementary information (ESI) available. See DOI: https://doi.org/10.1039/d5nr00385g

minimal changes in the range of 8–14 μm. Therefore, maximizing emissivity control in the 3–5 μm band can alter the thermal radiation characteristics of camouflaged objects, potentially confusing or misleading IR detectors, while ensuring that the thermal radiation characteristics in the 8–14 μm band remain consistent with the environment. Conversely, in the case of medium-temperature objects at around 70 °C, emissivity control mainly affects the range of 8–14 μm, necessitating a focus on different spectral ranges than that for low-temperature objects. In the case of high-temperature objects, the trend of thermal radiation characteristics in both the 3–5 and 8–14 μm bands is similar with emissivity changes. Achieving opposite changes in thermal radiation characteristics across these two bands can enhance the camouflage effect. Consequently, the associated thermal camouflage naturally demands tri-spectral independent manipulations. However, achieving decoupled tri-spectral emissivity within simple-structured materials remains challenging due to variations in the spectral properties and thermal stability of phase-change materials.[23]

The main challenges are decoupling modulation and maximizing the modulation depth in the thermal radiation of the target. One approach to overcome these issues is the integration of heterogeneous PCMs. Nevertheless, this may result in competition between the performance of different inclusions because of their unique phase-transition temperatures and spectral properties. Additionally, current thermal camouflage techniques that rely solely on emissivity modulation are impractical,[24,25] particularly in the case of significant temperature differences. Fig. 1b illustrates the range of T_r achievable solely through emissivity modulation for an ideal gray body model, which can only fluctuate between the ambient apparent temperature ($\varepsilon(\lambda) = 0$) and the blackbody temperature ($\varepsilon(\lambda) = 1$). This limitation makes it difficult to substantially alter T_r for low-temperature targets using emissivity modulation alone. Alternatively, active modulation combining temperature and emissivity modulation offers enhanced flexibility for thermal camouflage, providing disorientation capabilities.[26] Thus far, compatible control techniques to manage temperature and emissivity in a tri-spectrum remain a key challenge.

Guangwei Hu

Dr Guangwei Hu is Nanyang Assistant Professor in EEE of Nanyang Technological University (Singapore). His research interests are nanophotonics, including theory, modelling, and materials for bio-imaging, computations, photonic chips, energy and other applications. He has published more than 100 papers in journals including Nature (4), Science and others. His work has won the Top 10 Breakthrough in Physics of 2020 by Physics World, Optics and Photonics News (Year of Optics in 2021), China's Top 10 Breakthrough in Optics in 2021, and many others. He received Early Career Awards in Nanophotonics, MIT TR35 (China), Forbes U30 (Asia), 20th Anniversary Challenge Award from Optica Foundation, Rising Star of Light and various other awards.

Herein, we propose a tri-spectral decoupled heterogeneous phase-change integrated multilayer thermal emitter and a multi-mode camouflage approach. This heterogeneous phase-change integration emitter enables both programmable thermal camouflage for fixed-temperature targets and active deceptive programmable thermal camouflage by jointly modulating temperature and emissivity. The non-volatile PCM IST allows emissivity modulation through localized phase changes without additional energy supplement. After a phase change, IST exhibits metallic characteristics across the entire IR spectrum.[19] Also, inducing a local phase change in non-volatile phase-change materials by a large-area laser was mentioned in ref. 27 and 28, which provides the possibility for the preparation of large-area non-lithography devices. The volatile PCM VO_2 with a low phase change temperature allows temperature-dependent modulation. Because the durability of their phase change behavior over multiple cycles has been demonstrated,[19,29] integrating IST with VO_2 offers great flexibility and enables both confusing programmable camouflage for fixed-temperature targets and active deceptive programmable camouflage by modulating both temperature and emissivity. Optimized with a physics-guided intelligent algorithm, our structure could produce 65.5% VIS colors of the sRGB color gamut and over 80% independently dynamic emissivity modulation in the range of 3–5 μm and 8–14 μm by controlling the phase change in the VO_2 or IST material. In the case of constant-temperature objects, the local phase change in IST generates a confusing programmable camouflage pattern, effectively disrupting detection in both IR spectral bands. In contrast, active deceptive thermal camouflage can produce customized thermal radiation signatures by simultaneously adjusting the temperature and emissivity, where the maximum apparent temperature modulation depth is 105 °C, enabling the target to replicate the thermal characteristics of other objects and transmit deceptive infrared signals.

2. Results and discussion

2.1 General decoupled multispectral modulation principle

Firstly, we briefly discuss the basic principles of multi-spectral decoupling camouflage, including the characterization of VIS color and calculation of IR thermal radiation. VIS color is related to the VIS reflectance of opaque objects, and the CIE 1931 standard *xy* chrominance diagram is the common method for quantifying VIS color (ESI S1†). In the case of IR camouflage, the apparent temperature, T_r, is an important thermal radiation characteristic of the target with object temp-

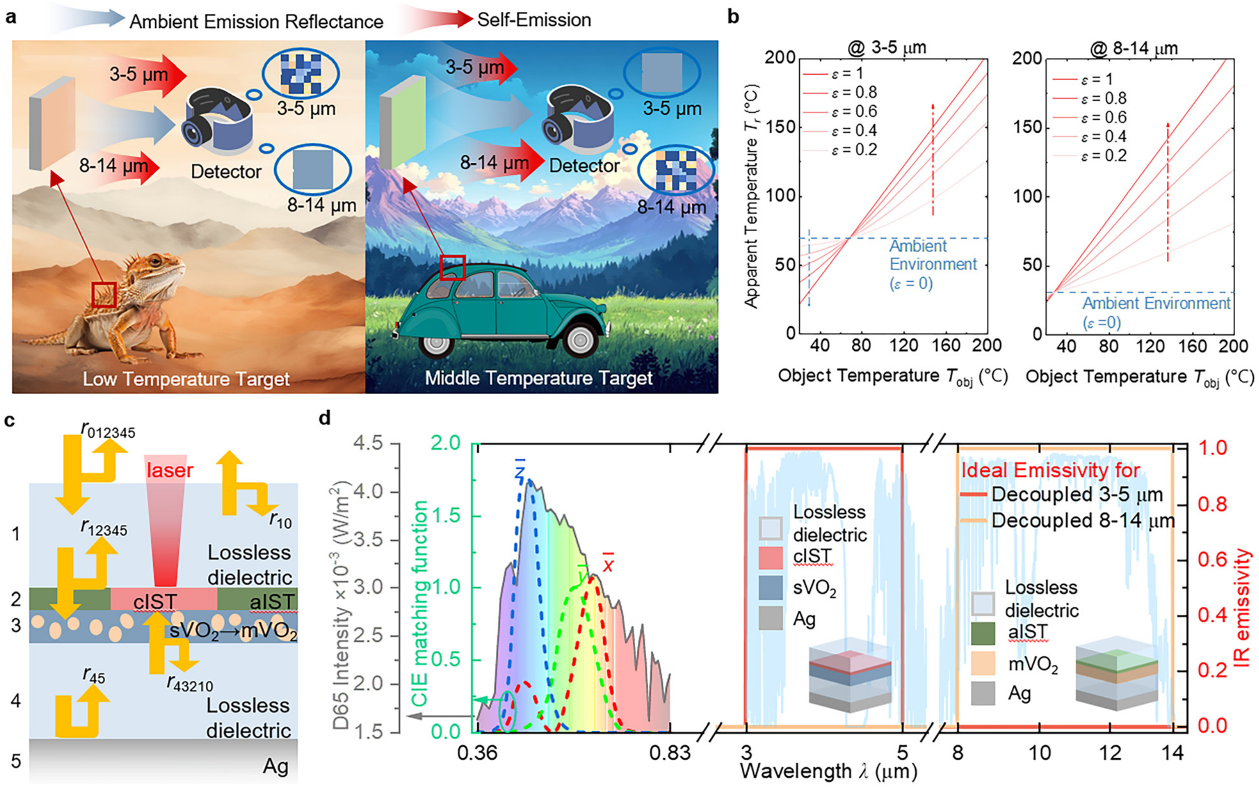

Fig. 1 Schematic of the decoupled camouflage principle and ideal spectral characteristics. (a) Potential applications of multi-band decoupled thermal camouflage for low-temperature and mid-temperature targets. The blue arrow represents the reflection of thermal radiation projected to the surface of the thermal camouflage device by the ambient environment, including the thermal radiation of the surrounding environment and solar radiation, and the red arrow represents the thermal self-emission of the thermal camouflage device. (b) Apparent temperature, T_r, as a function of emissivity, ε, and the object temperature, T_{obj}, is in the range of 3–5 μm and 8–14 μm. Here, we assume the device is a gray body, and the blue dash line is the apparent temperature of the ambient environment radiation when the target's emissivity is 0 according to eqn (1), and the red and blue dash dot lines are the emissivity modulation trends with increasing average emissivity for the corresponding spectral region. (c) Schematic of the heterogeneous phase-change material integrated thermal emitter. The green region and red region indicate the local phase-change process of IST *via* laser stimulation. The blue region and light orange region represent the uniform phase transition of VO$_2$ from sVO$_2$ to mVO$_2$ upon heating, and r_{ij} denotes the reflectance coefficient from the *i*th layer into the *j*th layer and the numbers on the left indicate the serial number of each layer. (d) D65 light source power density and the ideal decoupled IR emissivity the range of 3–5 μm and 8–14 μm, where the dash lines are CIE matching functions. The light blue lines represent atmospheric transmittance, indicating that 3–5 and 8–14 μm are the commonly used atmospheric windows for infrared detection with high infrared transmittance.

erature T_{obj}, which is obtained by referring to the standard blackbody radiation, as follows:

$$\int_{\lambda_{\min}}^{\lambda_{\max}} \frac{2\pi hc^2 \varepsilon_{\mathrm{detector}}(\lambda)}{\lambda^5\left(\exp\left(\frac{hc}{k_B \lambda T_r}\right)-1\right)}\mathrm{d}\lambda = \int_{\lambda_{\min}}^{\lambda_{\max}} \frac{2\pi hc^2 \varepsilon(\lambda)}{\lambda^5\left(\exp\left(\frac{hc}{k_B \lambda T_{\mathrm{obj}}}\right)-1\right)} + (1-\varepsilon(\lambda))\left(\frac{2\pi hc^2 \varepsilon_{\mathrm{amb}}(\lambda)}{\lambda^5\left(\exp\left(\frac{hc}{k_B \lambda T_{\mathrm{amb}}}\right)-1\right)} + I_{\mathrm{sun}}\right)\mathrm{d}\lambda \tag{1}$$

where h is the Planck constant, c is the speed of light in vacuum, λ is the wavelength, k_B is the Boltzmann constant, $\varepsilon(\lambda)$ is the spectral emissivity of the target, $\varepsilon_{\mathrm{amb}}(\lambda)$ and $\varepsilon_{\mathrm{detector}}(\lambda)$ are the ambient and the detector calibrated emissivity, respectively, which are both assumed to be 0.95 in this work. Besides, I_{sun} is the spectral solar radiation calculated by MODTRAN,[30] and the detailed setting parameters are shown in ESI S2.† It is worth noting that the variation in T_r is influenced not only by the emissivity of the target, $\varepsilon(\lambda)$, but also by the balance between the self-emitted thermal radiation, which depends on its temperature, and the environment and solar radiation. When the target has low temperature, the self-radiation intensity is lower than the direct solar radiation in the range of 3–5 μm. Therefore, in the radiation signal received by the detector, solar radiation occupies the main position, and the device with a higher emissivity will reflect lower solar radiation, and thus the infrared image displayed by the detector will be shown as a lower signal intensity. On the contrary, when the object temperature is sufficiently high, the self-radiation intensity is much higher than the direct solar radiation. Thus, the higher the emissivity of the object, the stronger the overall radiation signal. Many studies also considered the impact of atmospheric transmittance,[31,32] which is typically related to the distance between the detector and the camouflaged object. In thermal radiation image measurements in the laboratory, the atmospheric transmittance is nearly 1 due to the proximity. However, at greater distances, the absorption peaks of various gases in the infrared spectrum become significant, and the thermal radiation captured by the detector will be slightly lower than that emitted by the camouflaged object. We used MODTRAN to calculate the atmospheric transmittance at different distances, which can be seen in ESI S2.† In this work, we assumed the measurement is conducted under laboratory conditions and approximately ignored the impact of atmospheric transmittance.

Fabry–Pérot (F–P) resonance-based emitters have been widely adopted to enhance the emissivity in one or two IR detection regions.[23,33] A five-layer heterogeneously integrated emitter with IST (red layer) and VO_2 (light orange layer) was utilized, as shown in Fig. 1c. Given that IST and VO_2 have different phase-change properties, different phase-change processes can be realized at different temperatures and using different methods. IST exhibits a high phase-change temperature (>250 °C) and non-volatile phase-change properties. As a result, the gradually induced local phase change modulated by a laser, without requiring continuous energy input, can avoid interference from VO_2. The phase transition in VO_2 is homogeneous and volatile, beginning uniformly and gradually at around 68 °C. Consequently, the VO_2 phase transition can be controlled by maintaining a lower temperature, ensuring that it does not exceed the phase-change temperature of IST. When amorphous IST (aIST) varies to crystal IST (cIST) or semiconducting VO_2 (sVO_2) varies to metallic VO_2 (mVO_2), it creates two resonance nanocavities, causing multiple reflections of the incident light. Given that the reflectance phase shifts depend on the permittivity on both sides of the cavity, the significant difference in the permittivity after the phase change (ESI S3†) and structure optimization can help excite F–P resonance in various IR wavelength bands with different PCMs. Fig. 1c illustrates a schematic of the multilayer tri-spectral decoupling thermal emitter, where based on the above-mentioned differences in phase-change characteristics, IST and VO_2 are utilized for 3–5 μm and 8–14 μm emissivity modulation in Fig. 1d, respectively.

2.2 Structure design and optimization for infrared decoupled modulation

To realize the decoupled modulation of thermal radiation in the IR dual detection bands, as shown in Fig. 1d, we optimized the heterogeneous integration structure shown in Fig. 1c with the GPU transmission matrix method and genetic algorithm (GPU-TMM-GA) method.[34–36] The optimized variables are the thickness of each layer and the material of the IR lossless dielectric layer. Also, the associated fitness value F_{adopted} can be expressed as follows:

$$F_{\text{adopted}} = \max\left(\left|\bar{\varepsilon}_{3-5}^{\text{cs}} - \bar{\varepsilon}_{3-5}^{\text{as}}\right| - \left|\bar{\varepsilon}_{8-14}^{\text{cs}} - \bar{\varepsilon}_{8-14}^{\text{as}}\right| - \left|\bar{\varepsilon}_{8-14}^{\text{am}} - \bar{\varepsilon}_{8-14}^{\text{as}}\right| - \left|\bar{\varepsilon}_{3-5}^{\text{am}} - \bar{\varepsilon}_{3-5}^{\text{as}}\right|\right) \tag{2a}$$

$$\bar{\varepsilon} = \frac{\int_{\lambda_{\min}}^{\lambda_{\max}} \frac{2\pi hc^2 \varepsilon(\lambda)}{\lambda^5\left(\exp\left(\frac{hc}{k_B\lambda T}\right)-1\right)} \mathrm{d}\lambda}{\int_{\lambda_{\min}}^{\lambda_{\max}} \frac{2\pi hc^2}{\lambda^5\left(\exp\left(\frac{hc}{k_B\lambda T}\right)-1\right)} \mathrm{d}\lambda} \tag{2b}$$

where $\bar{\varepsilon}$ is the average emissivity, whose subscripts and superscripts indicate the spectral region and the phase states of both PCMs, respectively, 'cs' means cIST/sVO_2, 'am' means aIST/mVO_2, and 'as' means aIST/sVO_2. The first two components of F_{adopted} modulate the emissivity in the range of 3–5 μm through IST, while ensuring stable thermal radiation in the range of 8–14 μm. In contrast, the latter two components regulate the emissivity in the range of 8–14 μm through VO_2, without compromising thermal radiation in the range of 3–5 μm. Ge and ZnS were utilized as alternative IR lossless materials, the permittivity of which was obtained from ref. 37–39. The permittivity of IST and VO_2 was obtained from ref. 19, 40 and 41 Because the trend of the temperature-dependent metallization fraction f_{mVO_2} is not the same during the heating and cooling process,[42] the Maxwell–Garnett effect medium theory was adopted to calculate the permittivity, which is detailed in ESI S4.†[43] The Ag substrate is sufficiently thick to ensure zero transmittance,[44] and according to Kirchhoff's law,[45] the spectral absorptance $\alpha(\lambda)$ is equal to the spectral emissivity $\varepsilon(\lambda)$.

Continuous programmable modulation of emissivity relies on the temperature-dependent phase-change process of VO_2 and controlling the local phase change of IST. Fig. 2a shows in detail how these two methods are used to decouple and regulate the thermal radiation characteristics of the two IR detection bands. With the optimized thicknesses of h_1 = 225 nm, h_2 = 62 nm, h_3 = 34 nm, and h_4 = 467 nm, and using Ge and ZnS as the top and middle dielectric layers, Fig. 2b illustrates the excellent average emissivity modulation depth $\bar{\varepsilon}_{3-5}$ of nearly 90% when only aIST fully changes to cIST, and average emissivity modulation depth $\bar{\varepsilon}_{8-14}$ of 76% when sVO_2 fully transitions to mVO_2. Both excellent emissivity modulation characteristics remained effective at large oblique incident angles, as shown in Fig. 2c. We verified the reliability of the calculation results in ESI S5,† and this tri-spectral decoupled camouflage can be scaled up for large-area fabrication by magnetron sputtering or electron beam evaporation, as previously described in ref. 46–48. By independently controlling f_{mVO_2} and f_{cIST}, Fig. 2d demonstrates the continuous programmable modulation of polarization-averaged average emissivity calculated by an open-source rigorous coupled wave analysis method code package,[49] which is verified in ESI S5.† Programmable continuous modulation of ε_{3-5} can be achieved by adjusting the grating width L_{cIST} through lasers due to the non-volatile phase-change property of IST.[19,50] The fill factor, f_{cIST}, can be expressed as $f_{\text{cIST}} = L_{\text{cIST}}/\Lambda$. Also, in the phase-change process of VO_2, the metallization fraction, f_{mVO_2}, can be controlled by temperature regu-

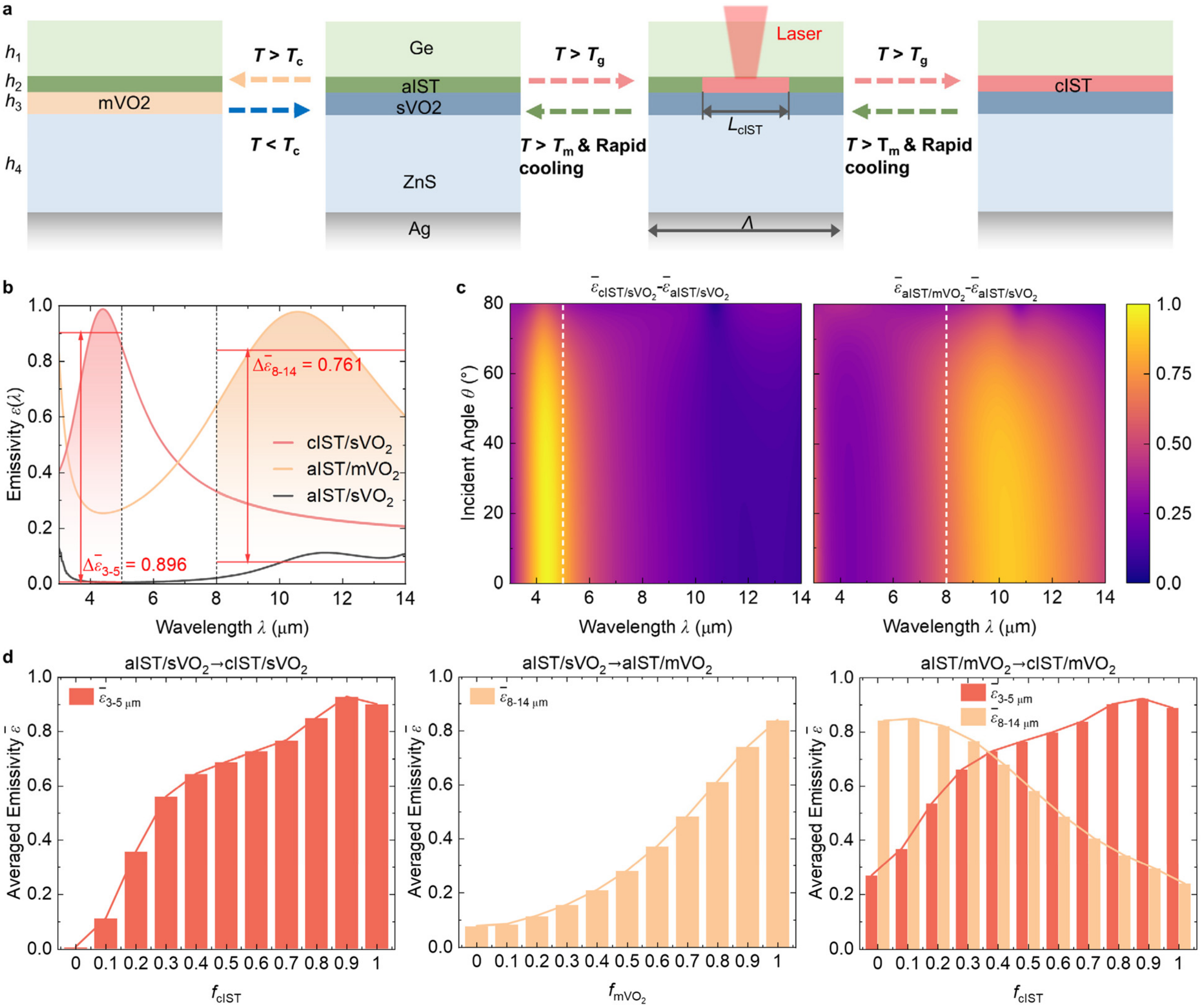

Fig. 2 Emissivity modulation for an optimized structure. (a) Spectral emissivity before and after full phase change. h_1–h_4 are the thickness of each layer corresponding to Fig. 1c. (b) Polarization-averaged averaged emissivity difference before and after phase change in IST and VO$_2$ at different incident angles. (c) Phase-change mechanism of VO$_2$ and method for realizing a local phase change in IST using laser, where T_c (68 °C) is the phase-change temperature of VO$_2$, and there will be hysteresis behavior during the heating and cooling procedure. Here, T_g (250 °C) and T_m are the glass transition temperature and melting temperature of IST, respectively, L_{cIST} is the width of cIST gratings, and Λ = 3 μm is the periodic width. (d) Polarization-averaged average emissivity modulation by individually controlling the fill factor, f_{cIST}, or f_{mVO_2}.

lation. However, when T_{obj} is a high temperature above the phase-change temperature of VO$_2$ and below the phase-change temperature of IST, gradually increasing f_{cIST}, $\bar{\varepsilon}_{3-5}$ is enhanced, while $\bar{\varepsilon}_{8-14}$ decreases, which is due to the thickness of the cIST layer exceeding its skin depth.

The phase shifts shown in Fig. 3a offer further insight into the decoupled IR emissivity modulation mechanism. Due to the lossless dielectric property of aIST and sVO$_2$, incident light is largely reflected by the Ag substrate, resulting in broadband and high reflectance characteristics. However, when aIST or sVO$_2$ individually change its phase to cIST or mVO$_2$, respectively, the F–P resonance is primarily excited in top resonance cavity 1. The phase shift results in three states (aIST/sVO$_2$, cIST/sVO$_2$, and aIST/mVO$_2$), as detailed in ESI S6.† Fig. 3b and c depict the spectral emissivity $\varepsilon(\lambda)$ as a function of thickness h_1 and h_4. When aIST undergoes a phase change to cIST, the peak emissivity in the range of 3–5 μm linearly red-shifts with an increase in h_1, but remains unaffected by variations in h_4 due to the thicker h_2 layer exceeding the skin depth of cIST, confining F–P resonance to the top cavity. Conversely, when sVO$_2$ transitions to mVO$_2$, the F–P resonance remains in top cavity 1, but given that the h_3 of mVO$_2$ is smaller than its skin depth in the range of 8–14 μm, variations in h_4 (as in h_1) affect the reflectance phase, shifting the resonance peak in the range of 8–14 μm. The decoupled resonance wavelengths with different thicknesses h_1 and h_4 in Fig. 3b and c, respectively, indicated by grey stars, align closely with the calculated emissivity peaks, confirming our theoretical model.

To demonstrate the effect of the decoupled modulation of IR emissivity on IR thermal camouflage based on the above-

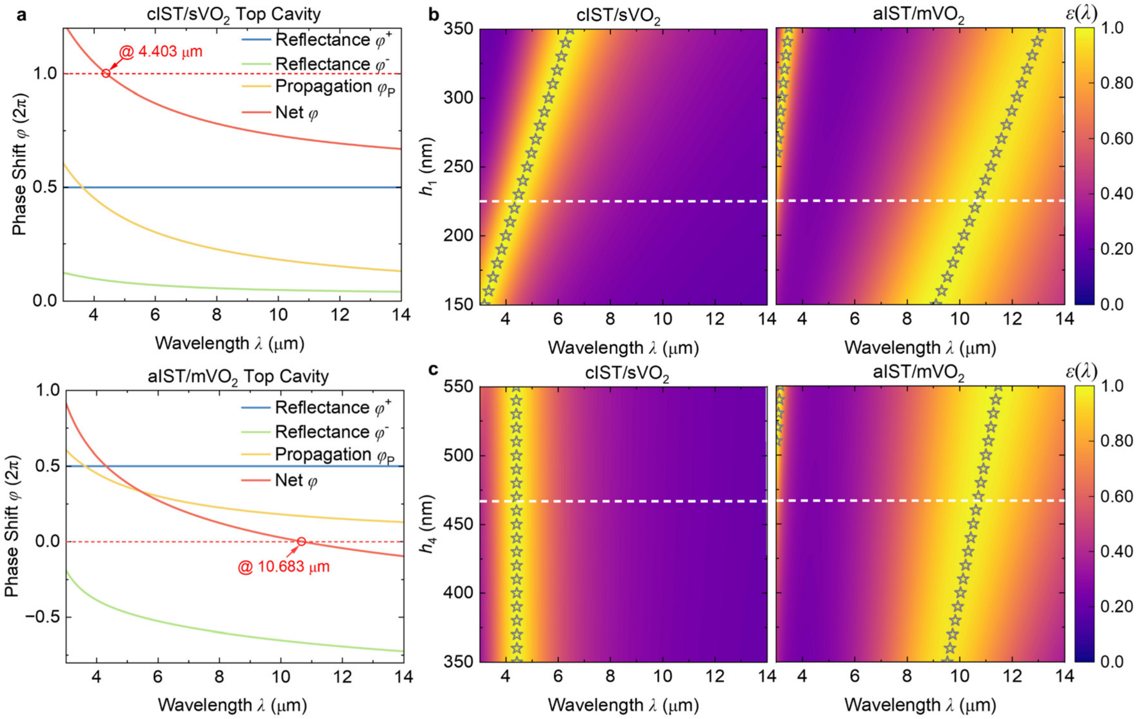

Fig. 3 Net phase shift and spectral emissivity as a function of h_1 and h_4. (a) Phase shift at the top cavity under different phase-change states. (b) Spectral emissivity with different thicknesses of h_1 under different phase states, where the grey stars are the predicted F–P resonance wavelengths and the white dashed lines mean the selected structure parameters. (c) Spectral emissivity with different thicknesses of h_4 under different phase states, where the grey stars are the predicted F–P resonance wavelengths and the white dashed lines are the selected structure parameters.

mentioned methods, the quantitative apparent temperature, T_r, at various T_{obj} and different phase-change materials states are depicted in Fig. 4. When T_{obj} is either low (20–40 °C) or high (100–200 °C), VO$_2$ in the heterogeneous phase-change material integrated thermal camouflage device remains in the amorphous or crystalline phase, with emissivity control determined by f_{cIST}. Fig. 4a shows the theoretical T_r as a function of f_{cIST} and T_{obj} for low-temperature targets in the 3–5 and 8–14 μm regions, where we select three T_{obj} samples as examples, as indicated by the lines. Their detailed T_r variations are shown in the right figure in Fig. 4a. As f_{cIST} increases, the theoretical T_r in the range of 3–5 μm gradually decreases, while the theoretical T_r in the range of 8–14 μm shows minimal change. For example, with line 1 (T_{obj} = 22.5 °C), as f_{cIST} increases from 0 to 0.8, T_r in the range of 3–5 μm decreases from 69.5 °C to 38.8 °C, achieving a modulation of up to 30.7 °C. This is because the self-radiation intensity of the low-temperature camouflaged targets in the range of 3–5 μm is much lower than that of the ambient and solar radiation (shown in ESI S2†). In contrast, in the 8–14 μm spectral region, the intrinsic thermal radiation intensity is comparable to the environment and solar radiation, resulting in minimal change. In the case of the high-temperature target, as depicted in Fig. 4b, an increase in f_{cIST} results in a gradual increase in emissivity in the range of 3–5 μm, while concurrently suppressing emissivity in the range of 8–14 μm, as shown in Fig. 2d. The apparent temperature T_r in line 3 increases from 123.9 °C to 171.7 °C in the range of 3–5 μm and decreases from 166.2 °C to 81.7 °C in the range of 8–14 μm. These results demonstrate that our heterogeneous phase-change integration camouflage devices can independently modulate two IR detection bands, supporting distinct camouflage effects and establishing a basis for 'thermal mosaic camouflage'. However, the range of T_r modulation achievable by adjusting the emissivity for targets at a fixed temperature is limited, especially when the self-emitted radiation of the target is comparable to the environment and solar radiation, which limits the tunable range of thermal radiation properties for targets at certain temperatures. For example, line 3 in Fig. 4a can only achieve 70.0% of the apparent temperature regulation depth of line 1 in the range of 3–5 μm, and line 1 in Fig. 4b can only achieve 64.2% and 67.9% of the apparent temperature regulation of line 3 in the range of 3–5 μm and 8–14 μm, respectively, showing a smaller modulation depth compared to other temperature targets.

In contrast, as T_{obj} increases from 40 °C to 100 °C, the temperature-dependent phase change in VO$_2$ creates a synergistic effect between emissivity and temperature, which allows the emitter to achieve an apparent temperature that can be tuned from the smallest to the largest within this temperature range. Fig. 4c illustrates that with IST in an amorphous state, T_r significantly shifts from 35 °C to 90 °C in the range of 8–14 μm, achieving a modulation of up to 55 °C. Alternatively,

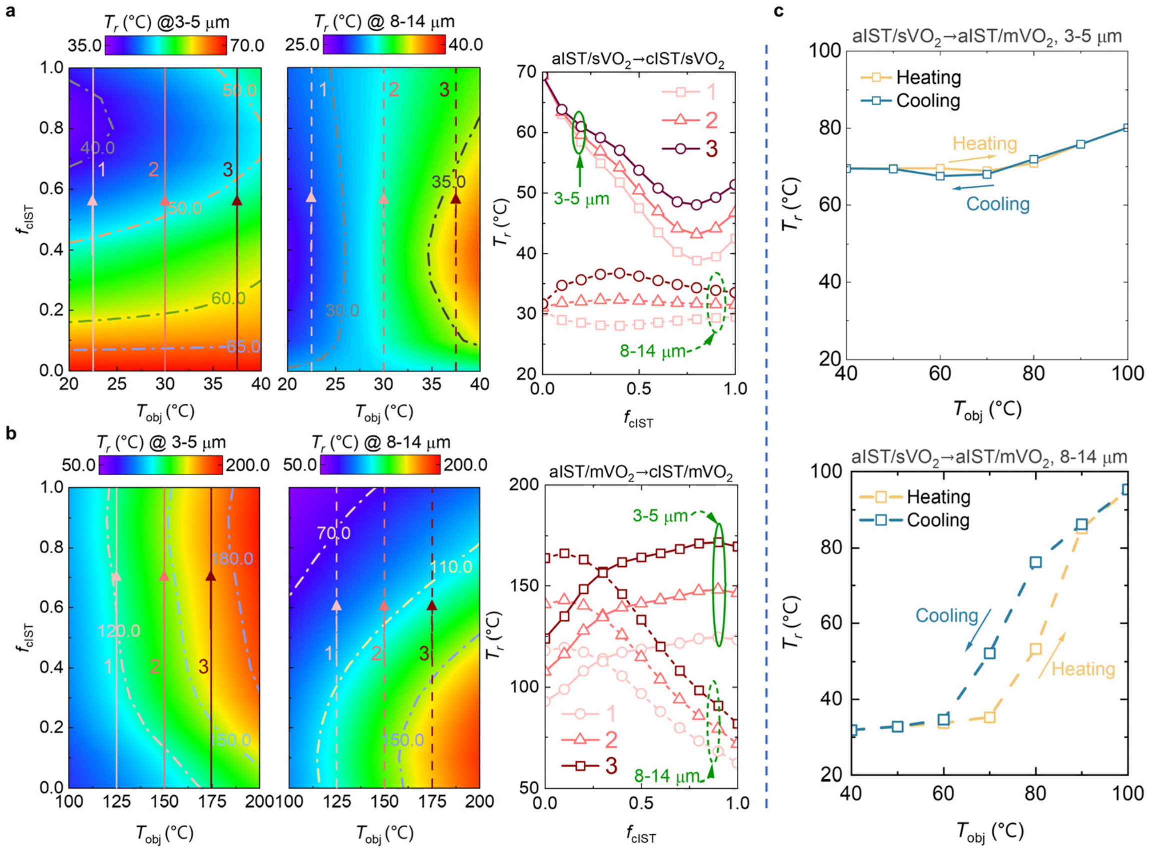

Fig. 4 Thermal radiation characteristic modulation of constant temperature target and schematic of passive camouflage modes. (a) Theoretical T_r as a function of f_{cIST} and T_{obj} from 20 °C to 40 °C, where the three lines represent three examples at a constant object temperature of 22.5 °C, 30 °C and 37.5 °C. The right figure represents how T_r in the range of 3–5 μm and 8–14 μm changes with f_{IST} for the three examples. (b) Theoretical T_r as a function of f_{cIST} and T_{obj} from 100 °C to 200 °C above the phase-change temperature of VO₂, where the three lines represent examples at a constant object temperature of 125 °C, 150 °C and 175 °C. The right figure represents how T_r in the range of 3–5 μm and 8–14 μm changes with f_{IST} for the three examples. (c) Theoretical T_r as a function of average emissivity $\bar{\varepsilon}$ and T_{obj} from 40 °C to 100 °C when IST is amorphous and the phase state of VO₂ is temperature dependent, where the yellow line indicates the variation in the average emissivity during the heating process and the blue line indicates the variation in the average emissivity during the cooling process.

it remains nearly close to the ambient apparent temperature (almost 70 °C) in the 3–5 μm region. This combination enables the active and significant modulation of thermal radiation properties across different camouflage cells. It is worth anticipating that this concept introduces a new approach for achieving active deceptive IR camouflage by integrating an emitter with a temperature-controlled device, even allowing the creation of false IR images that do not naturally exist.

2.3 VIS and IR decoupled modulation and programmable camouflage

It is clear that the decoupled IR thermal emissivity modulation mainly relies on the switching of the F–P resonance, which only imposes the phase shift in the resonance cavity, meeting the requirements for the resonance to be excited, but does not impose strict requirements on the choice of the material and thickness of the dielectric layers. ZnS and Ge have huge dielectric function differences in the VIS band. Fig. 5a directly illustrates a schematic structure for color customization based on IR dual-band decoupled modulation, with the two top dielectric layers increasing the range of color variation. To realize VIS customization, the fitness value F_{adopted} is modified as follows:

$$F_{\text{adopted\_IR}} = \max\left(\left|\bar{\varepsilon}^{\text{cs}}_{3-5} - \bar{\varepsilon}^{\text{as}}_{3-5}\right| - \left|\bar{\varepsilon}^{\text{cs}}_{8-14} - \bar{\varepsilon}^{\text{as}}_{8-14}\right| + \left|\bar{\varepsilon}^{\text{am}}_{8-14} - \bar{\varepsilon}^{\text{as}}_{8-14}\right| - \left|\bar{\varepsilon}^{\text{cs}}_{3-5} - \bar{\varepsilon}^{\text{as}}_{3-5}\right|\right) \tag{3a}$$

$$F_{\text{adopted\_vis}} = \min\left(\sqrt{(x - x_{\text{aim}})^2 + (y - y_{\text{aim}})^2}\right) \tag{3b}$$

where x_{aim} and y_{aim} are the aim coordinates in the CIE 1931 standard xy chrominance diagram. Fig. 5b shows the range of colors that can be achieved by judiciously choosing the material and thickness of each dielectric layer. The structural color characteristics of the heterogeneous phase-change inte-

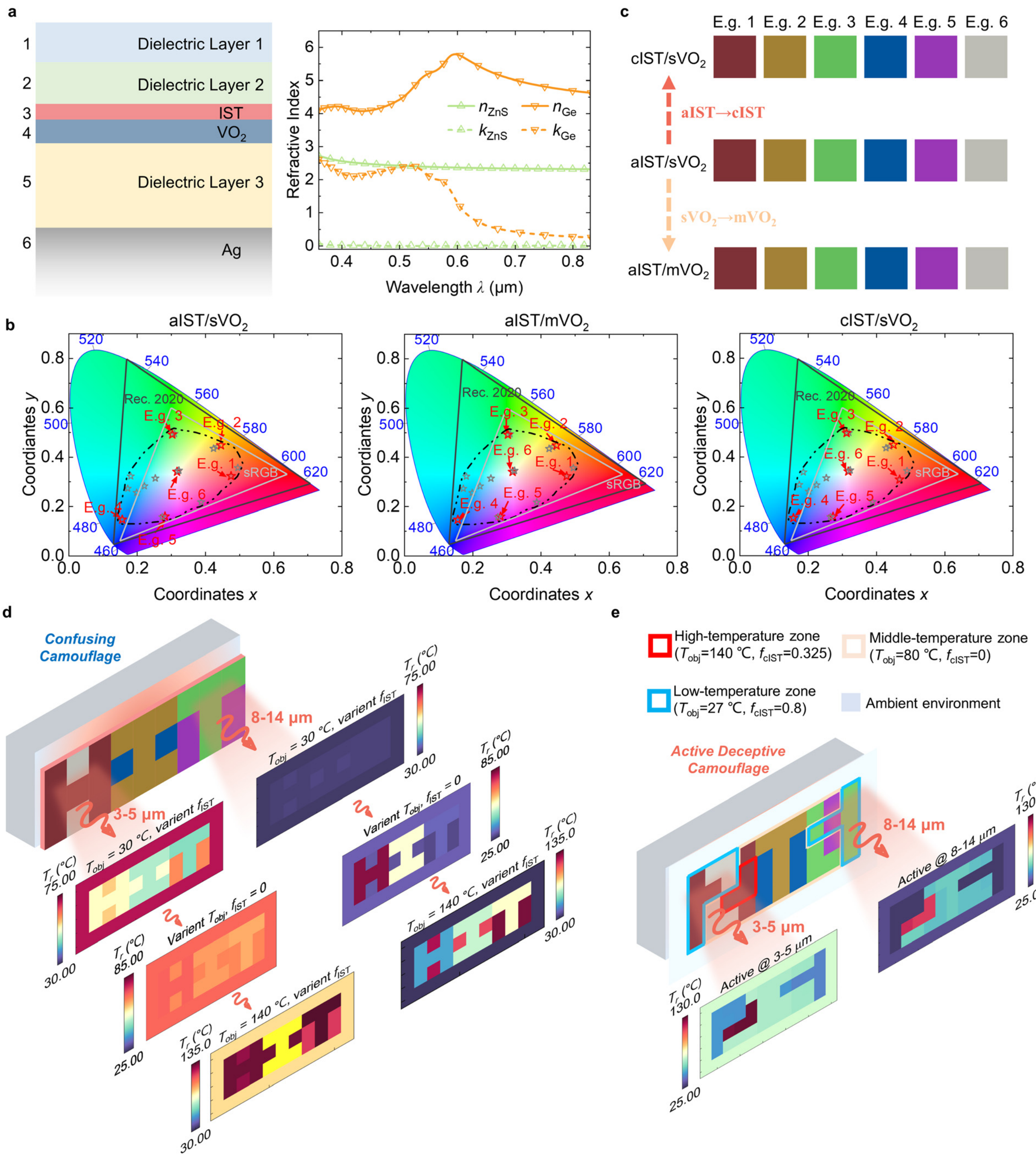

Fig. 5 Decoupled VIS-IR modulation and schematic of colored passive and deceptive camouflage modes. (a)Schematic of the six-layer structure of VIS and IR decoupled camouflage devices, and the refractive index of ZnS and Ge. (b) Color region before and after IST and VO$_2$ phase change process in E.g. 1–6 as six selected examples, where the dark and grey lines are the Rec. 2020 and sRGB color gamut, respectively. (c) Detailed color characteristics of the six examples in b. (d) Example of confusing camouflage in different temperature regions, where the 'HIT' VIS images are composed of the six examples in b, the left is the IR images in the range of 3–5 μm and the right is the IR images in the range of 8–14 μm under different consistent temperatures or different fill factors, f_{IST}, in different cells. (e) Example of active deceptive camouflage and 'NTU' VIS images are also composed of the six examples in b, and these IR images are created by controlling the temperature and f_{IST} of the different units. The areas enclosed within curves of different colors represent distinct temperatures and phase states.

gration devices can cover 65.5% of the sRGB color gamut, even surpassing the gamut range of sRGB in green and blue colors and enabling a broader and more nuanced range of color adjustments. The stability of the color is ensured by the small difference in the VIS permittivity of VO$_2$ and IST before and after the phase change and their thin thickness. Fig. 5c shows the color results of the six examples in Fig. 5b, whose detailed parameters, optical characteristics and robustness are shown in ESI S7.†

Using colored heterogeneous integration devices, we demonstrated programmable thermal camouflage in different confusing and active deceptive modes. Schematic illustrations of our defined confusing and deceptive programmable camouflage systems are shown in ESI S8.† Given that objects in complex environments have varying emissivity and temperatures, a mosaic-like camouflage pattern is more effective in blending with the actual environment.[51] We present an example of tri-spectral decoupling confusing camouflage by arranging and combining multiple cells with different emissivity to construct a 3 × 9 grid image of 'HIT'. Fig. 5d exhibits the IR images at low T_{obj} (30 °C) and high T_{obj} (140 °C) in the range of 3–5 μm and 8–14 μm. At this time, VO_2 is in the semiconductor and metallic state and the thermal radiation is controlled by the phase change states of IST. We set the fill factor, f_{cIST}, as 1.0 (red color), 0.8 (yellow color), 0.7 (green color), 0.4 (blue color), 0.3 (gray color) and 0.1 (purple color). Given that each camouflage cell is parallel and lies on the same plane, the angular coefficient between each plane is 0. Thus, we did not need to consider the radiative interactions between cells and could determine the corresponding apparent temperature distribution based on eqn (1) and the spectral emissivity of each cell at a specific f_{cIST}. In other words, the apparent temperature of each cell was independently calculated for each detection band, and arranging them by position resulted in the images shown in Fig. 5d and e. Due to the decoupled modulation of emissivity across the two detection bands, the IR T_{r} images exhibit noticeable differences. In the case of the low-temperature target shown in the first result in Fig. 5d, we could strategically configure and arrange camouflage cells with different f_{cIST} to display the desired "HIT" thermal image in the range of 3–5 μm. These cells exhibited a customized T_{r} based on their f_{cIST}. In practical scenarios, we can further adjust the proportion of each cell to create more complex camouflage patterns. This allows the depiction of IR images of other objects within the environment, better enhancing the adaptation to intricate surroundings. Meanwhile, in the range of 8–14 μm, the T_{r} image remains generally similar to the ambient temperature, demonstrating the capability to blend into a traditional cold background. Conversely, for the last high-temperature camouflage result in Fig. 5d, changes in the f_{cIST} cause the emissivity in the two bands to vary in opposite directions. This allows the camouflage device to create mosaic-like patterns in both bands, with each band exhibiting opposite apparent temperature trends, thereby potentially confusing detectors. The middle result in Fig. 5d exhibits the IR images when the temperature of the cell of E.g. 1–6 is 90 °C (red color), 80 °C (yellow color), 70 °C (green color), 50 °C (blue color), 40 °C (gray color), and 60 °C (purple color). The phase transition of VO_2 within the cell structure primarily affects the emissivity in the range of 8–14 μm, with minimal impact on the range of 3–5 μm. As a result, the IR image in the range of 8–14 μm can display a mosaic camouflage image of 'HIT', which differs from the environment, while appearing consistent with the environment in the range of 3–5 μm.

In contrast, the active deceptive programmable camouflage offers a broader range of control by simultaneously varying the temperature and emissivity of each unit, enabling customization of the IR image of different objects to mislead the detector. The temperature of each camouflage unit can be adaptively regulated using an independent thermoelectric heat source with PID control. They were spaced appropriately to minimize thermal conduction effects and ensure stability.[52] The active deceptive camouflage mode enables richer IR characteristics by combining temperature and emissivity modulation, creating complex thermal camouflage mosaics and false IR images in the range of 3–5 μm and 8–14 μm. As an example, we constructed a 4 × 10 grid image of 'NTU' by arranging and combining multiple units of E.g. 1–6. As shown in Fig. 5e, we divided the camouflage units into low, mid, and high-temperature zones to create distinct IR characteristics that mimic the surface of the object and its inside hot spots. The low-temperature zone employs lower temperatures and a higher fill factor, f_{cIST}, to blend with the environmental background. In contrast, the mid and high-temperature zones use higher temperatures and varying fill factor, f_{cIST}, to exhibit the desired high thermal radiation characteristics. The specific temperature and fill factor, f_{cIST}, of each zone are provided in the labels. By strategically adjusting the temperature and emissivity of each region, we demonstrate in Fig. 5e how the IR image of the letters 'NTU' can be transformed into a false tank IR signature through this synergistic approach. This tri-spectral decoupled thermal emitter with heterogeneous phase-change integration provides a viable way to achieve programmable thermal camouflage with large variations in different bands, and two PCMs with different phase change properties give the ability to achieve two modes of thermal camouflage, which has not been previously reported.

3. Conclusion

In summary, by integrating VO_2 and IST with different phase-change properties, rational structure design, and dielectric material selection, we proposed a tri-spectral decoupling multilayer thermal emitter to achieve two confusing and deceptive colored thermal camouflage methods. Utilizing dual-cavity F–P resonance, individual control of the phase change in IST or VO_2 enabled us to achieve an IR emissivity modulation amplitude of 89.6% in the range of 3–5 μm and 76.1% in the range of 8–14 μm, respectively, while preserving the low-emission properties in the other spectral bands. The programmable and continuous emissivity modulation could be achieved by changing the fill factor, f_{cIST}, and temperature. While maintaining an IR regulation depth above 80%, the emitter integrated with the heterogeneous phase-change materials could independently exhibit a broad VIS color characteristic, covering 65.5% of the sRGB gamut. Based on these emissivity modulation characteristics and the phase-change property of IST and VO_2, we demonstrated two different modes of thermal camouflage, enhancing the multiband capability. Through compatible modulation of temperature and emissivity, we could achieve spurious IR properties that simulate other objects, and the apparent temperature modulation depth is 105 °C. Our strategy *via* heterogeneous phase-change integration provides new ways to achieve programmable thermal camouflage with greater degrees of freedom. Future research should be devoted to practical experimental demonstrations.

Data availability

Data underlying the results presented in this paper are not publicly available at this time but may be obtained from the authors upon reasonable request.

Conflicts of interest

The authors declare that they have no known competing financial interests or personal relationships that could have appeared to influence the work reported in this paper.

Acknowledgements

This work was supported by the National Natural Science Foundation of China (No. 52227813), the China Scholarship Council (CSC202306120176), and the Fundamental Research Funds for the Central Universities (HIT.DZJJ.2023102). G. H. acknowledges the Nanyang Assistant Professorship Start-up Grant and A*STAR under its AME IRG Grant (Project No. M24N7c0081).

References

1 R. Hanlon, Cephalopod dynamic camouflage, *Curr. Biol.*, 2007, **17**, R400–R404.

2 J. Yang, X. Zhang, X. Zhang, L. Wang, W. Feng and Q. Li, Beyond the Visible: Bioinspired Infrared Adaptive Materials, *Adv. Mater.*, 2021, **33**, 2004754.

3 P.-C. Hsieh, S.-W. Chang, W.-H. Kung, T.-C. Hsiao and H.-L. Chen, Epsilon-near-zero thin films in a dual-functional system for thermal infrared camouflage and thermal management within the atmospheric window, *Mater. Horiz.*, 2024, **11**, 5578–5588.

4 P. Min, Z. Song, T. Wang, V. G. Ralchenko, Y. He and J. Zhu, Design strategy of a high-performance multispectral stealth material based on the 3D meta-atom, *Photonics Res.*, 2023, **11**, 1934–1944.

5 M. Pan, Y. Huang, Q. Li, H. Luo, H. Zhu, S. Kaur and M. Qiu, Multi-band middle-infrared-compatible camouflage with thermal management via simple photonic structures, *Nano Energy*, 2020, **69**, 104449.

6 Z. Fan, T. Hwang, S. Lin, Y. Chen and Z. J. Wong, Directional thermal emission and display using pixelated non-imaging micro-optics, *Nat. Commun.*, 2024, **15**, 4544.

7 C. Xu, G. T. Stiubianu and A. A. Gorodetsky, Adaptive infrared-reflecting systems inspired by cephalopods, *Science*, 2018, **359**, 1495–1500.

8 H. Liang, X. Zhang, F. Wang, C. Li, W. Yuan, W. Meng, Z. Cheng, Y. Dong, X. Shi, Y. Yan, H. Yi, Y. Shuai and Y. Long, Bio-inspired micropatterned thermochromic hydrogel for concurrent smart solar transmission and rapid visible-light stealth at all-working temperatures, *Light: Sci. Appl.*, 2024, **13**, 202.

9 H. Zhu, Q. Li, C. Tao, Y. Hong, Z. Xu, W. Shen, S. Kaur, P. Ghosh and M. Qiu, Multispectral camouflage for infrared, visible, lasers and microwave with radiative cooling, *Nat. Commun.*, 2021, **12**, 1805.

10 Z. Meng, B. Huang, S. Wu, L. Li and S. Zhang, Bio-inspired transparent structural color film and its application in biomimetic camouflage, *Nanoscale*, 2019, **11**, 13377–13384.

11 Y. Li, X. Bai, T. Yang, H. Luo and C.-W. Qiu, Structured thermal surface for radiative camouflage, *Nat. Commun.*, 2018, **9**, 273.

12 B. Gui, J. Wang, L. Zhang, Y. Zhu, Y. Jia, C. Xu, M. Yan, Z. Chu, J. Wang and S. Qu, Design of scene-adaptive infrared camouflage emitter based on Au-VO2-Al_2O_3-Au metamaterials, *Opt. Commun.*, 2022, **512**, 128016.

13 W. Hu, Z. Deng, P. Zhou, L. Huang, T. Wang, X. Wang and R. Gong, Dynamic selective emitter for low infrared signal over wide temperature range based on VO2, *Opt. Commun.*, 2024, **571**, 130868.

14 Z. RahimianOmam, A. Ghobadi, B. Khalichi and E. Ozbay, Adaptive thermal camouflage using sub-wavelength phase-change metasurfaces, *J. Phys. D: Appl. Phys.*, 2022, **56**, 025104.

15 Y. Guo, L. Zhu, S. Chen, S. Zhou, Q. Pan, J. Zhao and Y. Shuai, Dual-band polarized optical switch with opposite thermochromic properties to vanadium dioxide, *Appl. Phys. Lett.*, 2022, **121**, 201102.

16 M. Ono, K. Chen, W. Li and S. Fan, Self-adaptive radiative cooling based on phase change materials, *Opt. Express*, 2018, **26**, A777.

17 A. F. Heßler, I. Bente, M. Wuttig and T. Taubner, Ultra–Thin Switchable Absorbers Based on Lossy Phase–Change Materials, *Adv. Opt. Mater.*, 2021, **9**, 2101118.

18 Y. Su, Z. Deng, W. Qin, X. Wang and R. Gong, Adaptive infrared camouflage based on quasi-photonic crystal with Ge2Sb2Te5, *Opt. Commun.*, 2021, **497**, 127203.

19 A. Heßler, S. Wahl, T. Leuteritz, A. Antonopoulos, C. Stergianou, C.-F. Schön, L. Naumann, N. Eicker, M. Lewin and T. W. Maß, In3SbTe2 as a programmable nanophotonics material platform for the infrared, *Nat. Commun.*, 2021, **12**, 1–10.

20 Q. Chen, D. Lu, Q. Tianwei, X. Luo, M. Xu and P. Li, Optical nanoimaging of laser-switched phase-change plasmonic infrared antennas, *Opt. Lett.*, 2024, **49**, 1021–1024.

21 K. Xu, W. Yang and H. Ye, Thermal infrared reflectance characteristics of natural leaves in 8–14 μm region: Mechanistic modeling and relationships with leaf water content, *Remote Sens. Environ.*, 2023, **294**, 113631.

22 S. Ullah, A. K. Skidmore, A. Ramoelo, T. A. Groen, M. Naeem and A. Ali, Retrieval of leaf water content spanning the visible to thermal infrared spectra, *ISPRS J. Photogramm. Remote Sens.*, 2014, **93**, 56–64.

23 S. Zhou, S. Dong, Y. Guo, Y. Shuai, H.-X. Xu and G. Hu, Colored thermal camouflage and anti-counterfeiting with programmable In3SbTe2 platform, *Nanophotonics*, 2024, **13**, 945–954.

24 Y. Li, F. Wang, A. Zhang, Z. Fu, R. Su, T. Gao, Z. Wang and J. Guo, Performance of the Multilayer Film for Infrared Stealth based on VO2 Thermochromism, *J. Therm. Sci.*, 2024, **33**, 1312–1324.

25 Y. Bo, Q. Zhang, P. Bai, H. Cui, L. Liu, G. Wang, L. Wang, S. Yuan, Z. Zhou and R. Ma, Flexible active pixel-matrix ultrafast thermal camouflage using square-wave temperature, *Joule*, 2024, **8**, 2160–2169.

26 J. Huang, L. Yuan, J. Liao, Y. Wang, Y. Liu, C. Ji, C. Huang and X. Luo, Dynamic Infrared Radiation Regulator Enabling Positive and Reversible Modulation of Emissivity and Temperature, *Adv. Mater. Technol.*, 2024, 2400522.

27 M. Giteau, L. Conrads, A. Mathwieser, R. Schmitt, M. Wuttig, T. Taubner and G. T. Papadakis, Switchable Narrowband Diffuse Thermal Emission With an In3SbTe2–Based Planar Structure, *Laser Photonics Rev.*, 2024, 2401438.

28 L. Conrads, N. Honné, A. Ulm, A. Heßler, R. Schmitt, M. Wuttig and T. Taubner, Reconfigurable and Polarization-Dependent Grating Absorber for Large-Area Emissivity Control Based on the Plasmonic Phase-Change Material In3SbTe2, *Adv. Opt. Mater.*, 2023, **11**, 2202696.

29 K. Muramoto, Y. Takahashi, N. Terakado, Y. Yamazaki, S. Suzuki and T. Fujiwara, VO2-dispersed glass: A new class of phase change material, *Sci. Rep.*, 2018, **8**, 2275.

30 A. Berk, P. Conforti, R. Kennett, T. Perkins, F. Hawes and J. Van Den Bosch, in *MODTRAN® 6: A major upgrade of the MODTRAN® radiative transfer code, in: 2014 6th Workshop on Hyperspectral Image and Signal Processing: Evolution in Remote Sensing (WHISPERS)*, IEEE, 2014, pp. 1–4.

31 A. K. Osgouei, A. Ghobadi, B. Khalichi and E. Ozbay, A spectrally selective gap surface-plasmon-based nanoantenna emitter compatible with multiple thermal infrared applications, *J. Opt.*, 2021, **23**, 085001.

32 B. Khalichi, A. Ghobadi, A. K. Osgouei, Z. R. Omam, H. Kocer and E. Ozbay, Phase-change Fano resonator for active modulation of thermal emission, *Nanoscale*, 2023, **15**, 10783–10793.

33 S. K. Chamoli and W. Li, Visibly transparent multifunctional camouflage coating with efficient thermal management, *Opt. Lett.*, 2023, **48**, 4340–4343.

34 S. Zhou, Y. Guo, L. Zhu, Y. Liu, Q. Pan, Y. Shuai and G. Hu, Continuous programmable mid-infrared thermal emitter and camouflage based on the phase-change material In3SbTe2, *Opt. Lett.*, 2023, **48**, 4388–4391.

35 S. J. Byrnes, Multilayer optical calculations, *arXiv*, 2016, preprint, arXiv:1603.02720, DOI:DOI: 10.48550/arXiv.1603.02720.

36 N. C. Passler and A. Paarmann, Generalized 4 × 4 matrix formalism for light propagation in anisotropic stratified media: study of surface phonon polaritons in polar dielectric heterostructures, *J. Opt. Soc. Am. B*, 2017, **34**, 2128–2139.

37 M. R. Querry, *Optical constants of minerals and other materials from the millimeter to the ultraviolet*, Chemical Research, Development & Engineering Center, US Army Armament, 1998.

38 T. N. Nunley, N. S. Fernando, N. Samarasingha, J. M. Moya, C. M. Nelson, A. A. Medina and S. Zollner, Optical constants of germanium and thermally grown germanium dioxide from 0.5 to 6.6 eV via a multisample ellipsometry investigation, *J. Vac. Sci. Technol., B:Nanotechnol. Microelectron.:Mater., Process., Meas., Phenom.*, 2016, **34**, 061205.

39 J. H. Burnett, S. G. Kaplan, E. Stover and A. Phenis, Refractive index measurements of Ge, *Proceedings of SPIE Optics and Photonics*, 2016, **9974**, 222–232.

40 A. Barker Jr, H. Verleur and H. Guggenheim, Infrared optical properties of vanadium dioxide above and below the transition temperature, *Phys. Rev. Lett.*, 1966, **17**, 1286.

41 I. O. Oguntoye, S. Padmanabha, M. Hinkle, T. Koutsougeras, A. J. Ollanik and M. D. Escarra, Continuously Tunable Optical Modulation Using Vanadium Dioxide Huygens Metasurfaces, *ACS Appl. Mater. Interfaces*, 2023, **15**, 41141–41150.

42 J. Rensberg, S. Zhang, Y. Zhou, A. S. McLeod, C. Schwarz, M. Goldflam, M. Liu, J. Kerbusch, R. Nawrodt, S. Ramanathan, D. N. Basov, F. Capasso, C. Ronning and M. A. Kats, Active Optical Metasurfaces Based on Defect-Engineered Phase-Transition Materials, *Nano Lett.*, 2016, **16**, 1050–1055.

43 S. Chandra, D. Franklin, J. Cozart, A. Safaei and D. Chanda, Adaptive multispectral infrared camouflage, *ACS Photonics*, 2018, **5**, 4513–4519.

44 A. Ciesielski, L. Skowronski, M. Trzcinski and T. Szoplik, Controlling the optical parameters of self-assembled silver films with wetting layers and annealing, *Appl. Surf. Sci.*, 2017, **421**, 349–356.

45 J. R. Howell, M. P. Mengüç, K. Daun and R. Siegel, *Thermal radiation heat transfer*, CRC press, 2020.

46 J. Wang, Z. Wu, X. Sun, Z. Tang, C. Wang, F. Yu, Z. Zhao, J. Mao, Q. Zhang and F. Cao, Multi-band compatible camouflage enabled by phase transition modulation of flexible GST films, *Chem. Eng. J.*, 2024, **499**, 156128.

47 M. Li, D. Liu, H. Cheng, L. Peng and M. Zu, Manipulating metals for adaptive thermal camouflage, *Sci. Adv.*, 2020, **6**, eaba3494.

48 X. Feng, M. Pu, F. Zhang, R. Pan, S. Wang, J. Gong, R. Zhang, Y. Guo, X. Li and X. Ma, Large–area low–cost

multiscale–hierarchical metasurfaces for multispectral compatible camouflage of dual–band lasers, infrared and microwave, *Adv. Funct. Mater.*, 2022, **32**, 2205547.

49 C. Kim and B. Lee, TORCWA: GPU-accelerated Fourier modal method and gradient-based optimization for metasurface design, *Comput. Phys. Commun.*, 2023, **282**, 108552.

50 X. Lyu, A. Heßler, X. Wang, Y. Cao, L. Song, A. Ludwig, M. Wuttig and T. Taubner, Combining Switchable Phase-Change Materials and Phase-Transition Materials for Thermally Regulated Smart Mid-Infrared Modulators, *Adv. Opt. Mater.*, 2021, **9**, 2100417.

51 I. Chang, T. Kim, N. Lee, J. Nam, J.-S. Lim, M. Yun and H. H. Cho, Multispectral Optical Confusion System: Visible to Infrared Coloration with Fractal Nanostructures, *ACS Appl. Mater. Interfaces*, 2022, **14**, 28337–28347.

52 J. Guo, G. Xu, D. Tian, Z. Qu and C.-W. Qiu, A Real-Time Self-Adaptive Thermal Metasurface, *Adv. Mater.*, 2022, **34**, 2201093.